10

Role of Welding Parameters in Determining the Geometrical Appearance of Weld Pool

R. Kovacevic

Z. N. Cao

Y. M. Zhang

Center for Robotics and Manufacturing Systems, University of Kentucky, Lexington, KY 40506

A three-dimensional numerical model is developed to describe the fluid flow and heat transfer in weld pools. Both full penetration and free deformation of the top and bottom weld pool surfaces are considered. Temperature distribution and fluid flow field are obtained. In order to analyze the influence of welding parameters on the geometrical appearance of weld pools, a normalized model is developed to characterize the geometrical appearance of weld pools. It is found that welding current can significantly affect the geometrical shape. When welding current increases, the curvature of the pool boundary at the trailing end increases. The effect of the welding speed on the geometrical appearance is slight, although its influence on the pool size is great. In the interest range of arc length (from 1 mm to 4 mm), the arc length can affect both the size and the shape of the weld pool. However, compared with the welding current and speed, its influences are much weaker. GTA welding experiments are performed to verify the validity of the numerical models. The appearance of weld pools was obtained by using machine vision and a high-shutter speed camera. It is found that the calculated results have a good agreement with the experimental ones.

1 Introduction

A series of studies has demonstrated that the grain structure of the weld metal plays a fundamental role in determining the mechanical properties of the joint [1–3]. Also, the microstructure of a weldment is primarily affected by the geometries of weld pools [4–6]. Thus, the mechanical properties of the joint depend directly on the geometry of the weld pool [7, 8]. In fact, the solidification of the weld pool metal is usually considered to be a nucleation and growth process. The nucleation is first formed on the solid-liquid interface. Then, grains grow along the maximum temperature gradient direction, i.e., along the direction normal to the weld pool boundary. As shown in Fig. 1(a), at low heat inputs and welding speeds, the weld pool becomes elliptical in shape, and, therefore, the columnar grains grow along the welding direction. At high heat inputs and welding speeds, on the other hand, a teardrop shaped weld pool forms and the resulting columnar grains are straight, as illustrated in Fig. 1(b). Therefore, welding parameters can affect the grain structure of the weld metal through its influence on the geometry of the weld pool. Hence, in order to acquire the desired mechanical properties, the roles of the welding parameters in determining the geometrical appearance of the weld pool must be studied.

The understanding of the roles will also play a fundamental part in the weld penetration control which has been one of the major research interests of the authors [9, 10]. It is known that the top-side sensing and control of the weld penetration, which is specified by the penetration depth and back-side bead width of the weld pool for the partial and full penetration respectively, are among the most important research issues in automated welding. However, both the penetration depth and back-side bead width can not be directly viewed using top-side sensors. Indirect methods, such as pool oscillation and infrared sensing, have to be used. It is known that the weld pool can provide abundant important information about the welding process. A skilled human operator can estimate the weld penetration by observing the weld pool. However, the sensing of the weld pool is difficult. As an alternative, the authors have sensed and controlled the sag geometry behind the weld pool [10]. Because of the recent development in the sensing technology, clear images of the weld pools have been acquired using a high shutter speed camera assisted with pulsed laser illumination [11]. A real-time image processing algorithm has been developed to extract the geometry of the weld pool on-line [12]. Based on numerous accurate measurements of the weld pools, it was found that the back-side bead width (status of the full penetration) can be determined from the measured parameters of the weld pool using a neural-network [13, 14]. In order to acquire the desired weld penetration, the geometry of the weld pool needs to be controlled. Thus, the correlation between the welding parameters and geometrical parameters of the weld pool must be understood.

Our research interest has been focused on the critical root pass where the full penetration is usually required. Although many numerical models have been established to determine heat transfer and fluid flow in the weld pool [15–20], the fully penetrated weld pools with free top and bottom surface have not been addressed. In this study, the geometry of the weld pool is characterized by the proposed parameters of the weld pool. A three-dimensional-numerical model is developed to calculate the fluid and heat transfer in the weld pool. Free top and bottom surfaces are used in the numerical model. The experimental verification of the numerical model is done. Based on the calculated weld pools, the roles of the welding parameters in determining the geometry of the weld pool are analyzed.

2 Numerical Model of Weld Pool

2.1 Governing Equations. In order to develop the numerical model, the process is defined as follows. The arc is regarded as a spatially distributed heat, current, and pressure flux source. Heat transfer and fluid flow occur in the weld pool. The following additional assumptions have been adopted for further simplification:

(1) The flow is Newtonian, incompressible, and laminar.
(2) Heat, current, and pressure distributions of the arc have Gaussian characteristics.
(3) Physical properties are constant.

Contributed by the Materials Division for publication in the JOURNAL OF ENGINEERING MATERIALS AND TECHNOLOGY. Manuscript received by the Materials Division June 11, 1995; revised manuscript received December 24, 1995. Associate Technical Editor: K. S. Chan.

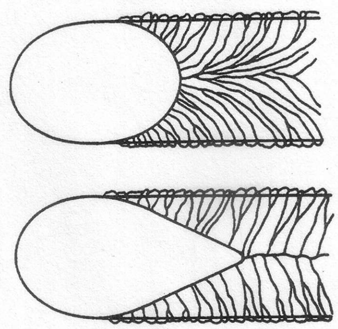

Fig. 1 Effect of welding parameters on grain structure [4]. (a) Low heat input and welding speed; (b) high heat input and welding speed.

It should be pointed out that when the pool surface is significantly deformed, the heat, current, and pressure distributions of the arc may not be exactly the Gaussian. However, in our calculation, the maximum welding current is 160 A. The surface deformation is not severe. Hence, the Gaussian distributions are still used in our calculation.

In this study, the coordinate system (x, y, z) is attached to the torch. The symmetric axis of the electrode is selected as the z axis. The work bottom surface is used to define the $x - y$ plane and the torch travels along the x axis. The governing equations, described by the continuity equation, the momentum equation, and the energy equation for quasi-steady state velocity and temperature fields in the workpiece, may be written as follows:

$$\frac{\partial u}{\partial x} + \frac{\partial v}{\partial y} + \frac{\partial w}{\partial z} = 0 \quad (1)$$

$$\rho\left[(u - u_0)\frac{\partial u}{\partial x} + v\frac{\partial u}{\partial y} + w\frac{\partial u}{\partial z}\right] = F_x - \frac{\partial P}{\partial x} + \mu\left(\frac{\partial^2 u}{\partial x^2} + \frac{\partial^2 u}{\partial y^2} + \frac{\partial^2 u}{\partial z^2}\right) \quad (2)$$

$$\rho\left[(u - u_0)\frac{\partial v}{\partial x} + v\frac{\partial v}{\partial y} + w\frac{\partial v}{\partial z}\right] = F_y - \frac{\partial P}{\partial y} + \mu\left(\frac{\partial^2 v}{\partial x^2} + \frac{\partial^2 v}{\partial y^2} + \frac{\partial^2 v}{\partial z^2}\right) \quad (3)$$

$$\rho\left[(u - u_0)\frac{\partial w}{\partial x} + v\frac{\partial w}{\partial y} + w\frac{\partial w}{\partial z}\right] = F_z - \frac{\partial P}{\partial z} + \mu\left(\frac{\partial^2 w}{\partial x^2} + \frac{\partial^2 w}{\partial y^2} + \frac{\partial^2 w}{\partial z^2}\right) \quad (4)$$

$$\rho C_p\left[(u - u_0)\frac{\partial T}{\partial x} + v\frac{\partial T}{\partial y} + w\frac{\partial T}{\partial z}\right] = \frac{\partial}{\partial x}\left(K\frac{\partial T}{\partial x}\right) + \frac{\partial}{\partial y}\left(K\frac{\partial T}{\partial y}\right) + \frac{\partial}{\partial z}\left(K\frac{\partial T}{\partial z}\right) \quad (5)$$

Where u, v, and w represent the x, y, and z directional velocities, respectively. u_0 is the welding speed, K-thermal conductivity, ρ-density, μ-viscosity, C_p-specific heat, P-pressure, and T-temperature. F_x, F_y, and F_z are the components of the body force. The body force $\mathbf{F}$ is calculated using the electromagnetic and buoyancy force [20]:

$$\mathbf{F} = \mathbf{J} \times \mathbf{B} - \rho\beta\mathbf{g}(T - T_m) \quad (6)$$

Where $\mathbf{J}$ is the current density vector, $\mathbf{B}$-magnetic induction vector, β-coefficient of volume expansion, $\mathbf{g}$-gravitational acceleration vector, and T_m-melting temperature.

2.2 Boundary Conditions

(i) Pool Surface Deformation. The molten pool is distorted by the gravitational force and arc pressure. The surface tension acts to support the molten pool. For the arc-pool interface, i.e., the top pool surface, the static force balance can be described by [21]:

Nomenclature

a, b = model parameters of geometrical appearance of the weld pool
$\mathbf{B}$ = magnetic induction vector
C_p = specific heat
F_x, F_y, F_z = components of body force
$\mathbf{g}$ = gravitational acceleration vector
I = welding current
$\mathbf{J}$ = current density vector
K = thermal conductivity
L = thickness of specimen
l = length of weld pool
L_{evap} = latent heat for the liquid-vapor phase-change
$\dot{m}$ = evaporation mass rate
$\mathbf{n}_b$ = normal unit vector to bottom surface
$\mathbf{n}_t$ = normal unit vector to top surface
p = liquid pressure
P_a = arc pressure
q_{conv} = heat loss from convection
q_{evap} = heat loss from evaporation
q_{radi} = heat loss from radiation
r = radial distance
T = temperature
T_m = melting temperature
T_∞ = ambient temperature
$\mathbf{t}_{bx}$ = tangential unit vector of bottom surface parallel to $x - z$ plane
$\mathbf{t}_{by}$ = tangential unit vector of bottom surface parallel to $y - z$ plane
$\mathbf{t}_{tx}$ = tangential unit vector of top surface parallel to $x - z$ plane
$\mathbf{t}_{ty}$ = tangential unit vector of top surface parallel to $y - z$ plane
u = x-direction velocity
u_w = arc voltage
u_0 = welding speed
$\mathbf{V}_b$ = velocity vector of bottom surface
$\mathbf{V}_t$ = velocity vector of top surface
v = y-direction velocity
w = z-direction velocity
x, y, z = regular coordinate system
x_r, y_r = normalized coordinate system
μ = viscosity
μ_0 = magnetic permeability
ρ = density
β = coefficient of volume expansion
γ = surface tension
$\partial\gamma/\partial T$ = surface tension temperature coefficient
η = arc efficiency
σ = Stefan-Boltzmann constant
σ_j = arc current flux distribution parameter
σ_q = arc heat flux distribution parameter
ϵ = surface emittance
ϕ = shape function of top pool surface
ψ = shape function of bottom pool surface

$$P_a - \rho g\phi + c = -\gamma \frac{(1+\phi_y^2)\phi_{xx} - 2\phi_x\phi_y\phi_{xy} + (1+\phi_x^2)\phi_{yy}}{(1+\phi_x^2+\phi_y^2)^{3/2}} \quad (7)$$

where $z = L - \phi(x, y)$ is the top pool surface, L is the material thickness, γ is the surface tension, and $\phi_x = (\partial\phi/\partial x)$, $\phi_{xx} = (\partial^2\phi/\partial x^2)$, etc. The arc pressure P_a is determined using the following formula [22]:

$$P_a(x, y) = \frac{\mu_0 I^2}{4\pi\sigma_j} \exp\left(-\frac{x^2+y^2}{2\sigma_j^2}\right) \quad (8)$$

where I is the welding current, σ_j-arc current distribution parameter, and μ_0-magnetic permeability. When the weld pool is fully penetrated, the bottom pool surface is also deformed. On the bottom pool surface, the surface tension prevents the weld pool from being burnt-through. The balance between gravity and surface tension can be written as:

$$\rho g(\psi + L - \phi) - c = -\gamma \frac{(1+\psi_y^2)\psi_{xx} - 2\psi_x\psi_y\psi_{xy} + (1+\psi_x^2)\psi_{yy}}{(1+\psi_x^2+\psi_y^2)^{3/2}} \quad (9)$$

where $z = -\psi(x, y)$ is the bottom pool surface, and $\psi_x = (\partial\psi/\partial x)$, $\psi_{xx} = (\partial^2\psi/\partial x^2)$, etc. Exactly speaking, the liquid in the weld pool is compressible. However, in order to avoid complexity, it has frequently been assumed that the liquid is incompressible. In our calculation, this assumption is also used so that the difference between the liquid and solid densities is negligible. Hence, the constant c can be determined from the following constraint of constant volume:

$$\oiint \phi(x, y)dxdy - \oiint \psi(x, y)dxdy = 0 \quad (10)$$

Equation (7) and Eq. (9) have the following boundary conditions, respectively,

$$\phi(x, y) = 0, \quad \text{when} \quad T \le T_m \quad (11)$$

$$\psi(x, y) = 0, \quad \text{when} \quad T \le T_m \quad (12)$$

(ii) Top Surface.

$$-K\nabla T \cdot \mathbf{n}_t = \frac{\eta I u_w}{2\pi\sigma_q^2} \exp\left(-\frac{x^2+y^2}{2\sigma_q^2}\right) - q_{\text{conv}} - q_{\text{radi}} - q_{\text{evap}} \quad (13)$$

$$-\mu\nabla(\mathbf{V}_t \cdot \mathbf{t}_{tx}) \cdot \mathbf{n}_t = \frac{\partial\gamma}{\partial T} \nabla T \cdot t_{tx} \quad (14)$$

$$-\mu\nabla(\mathbf{V}_t \cdot \mathbf{t}_{ty}) \cdot \mathbf{n}_t = \frac{\partial\gamma}{\partial T} \nabla T \cdot t_{ty} \quad (15)$$

$$\mathbf{V}_t \cdot \mathbf{n}_t = 0 \quad (16)$$

where $\mathbf{n}_t$ is the normal unit vector of the top surface, u_w-arc voltage, σ_q-arc heat flux distribution parameter, η-arc efficiency, $\mathbf{V}_t$-velocity vector on the top surface, $\mathbf{t}_{tx}$-the tangential unit vector of the top surface parallel to the $x - z$ plane, $\mathbf{t}_{ty}$-the tangential unit vector of the top surface parallel to the $y - z$ plane, and $\partial\gamma/\partial T$-temperature coefficient of the surface tension. The heat loss due to convection, evaporation, and radiation can be written as:

$$q_{\text{conv}} = h(T - T_\infty) \quad (17)$$

$$q_{\text{evap}} = \dot{m} L_{\text{evap}} \quad (18)$$

$$q_{\text{radi}} = \sigma\epsilon(T^4 - T_\infty^4) \quad (19)$$

where h is the convection coefficient, σ-Stefan-Boltzman constant, ϵ-surface emittance, T_∞-ambient temperature, L_{evap}-latent heat for the liquid-vapor phase-change, and $\dot{m}$-evaporation mass rate. For a metal such as steel, $\dot{m}$ can be written as [23]:

$$\log(\dot{m}) = A - B/T - 0.5 \log T \quad (20)$$

where A and B are two constants depending on the used material.

(iii) Bottom Surface.

$$-K\nabla T \cdot \mathbf{n}_b = -q_{\text{conv}} - q_{\text{radi}} \quad (21)$$

$$-\mu\nabla(\mathbf{V}_b \cdot \mathbf{t}_{bx}) \cdot \mathbf{n}_b = \frac{\partial\gamma}{\partial T} \nabla T \cdot \mathbf{t}_{bx} \quad (22)$$

$$-\mu\nabla(\mathbf{V}_b \cdot \mathbf{t}_{by}) \cdot \mathbf{n}_b = \frac{\partial\gamma}{\partial T} \nabla T \cdot \mathbf{t}_{by} \quad (23)$$

$$\mathbf{V}_b \cdot \mathbf{n}_b = 0 \quad (24)$$

where $\mathbf{n}_b$ is the normal unit vector of the bottom surface, $\mathbf{V}_b$-velocity vector on the bottom surface, $\mathbf{t}_{bx}$-the tangential unit vector of the bottom surface parallel to $x - z$ plane, and $\mathbf{t}_{by}$-the tangential unit vector of the bottom surface parallel to the $y - z$ plane.

(iv) Front Surface.

$$u = v = w = 0 \quad (25)$$

$$T = T_\infty \quad (26)$$

(v) Rear Surface.

$$u = v = w = 0 \quad (27)$$

$$K\frac{\partial T}{\partial y} = -q_{\text{conv}} \quad (28)$$

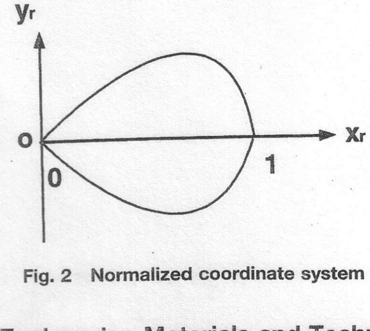

Fig. 2 Normalized coordinate system

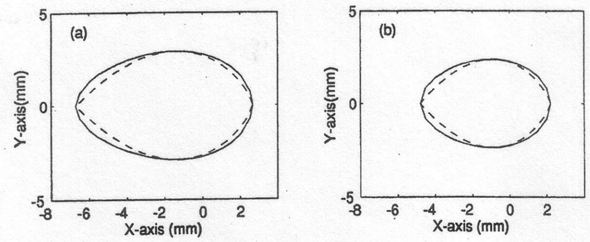

Fig. 3 Comparison between the numerical boundary and normalized one (– numerical, -- normalized). (*a*) 120A (*b*) 80A.

3 Normalization of Weld Pool Geometry Appearance

In order to study the geometry of the weld pool, the weld pool must be characterized by parameters. Although the pool length and width could provide a rough description of the geometry, a more accurate description is preferred.

We have proposed the following parametric model to describe the weld pool boundary in the normalized coordinate system $x_r o y_r$ (Fig. 2) [14]:

$$y_r = \mp a(1 - x_r)^b x_r \quad (a > 0, 1 \ge b > 0) \quad (29)$$

where $x_r = x/l$, $y_r = y/2l$, l is the length of the weld pool, and a and b are the model parameters. It has been shown (Fig. 3)

Table 1 Parameters used in computation

$C_p = 630$ J/kg·K	$\mu = 6 \times 10^{-3}$ kg/m·s
$h = 80$ W/m^2·K	$\mu_0 = 1.26 \times 10^{-6}$ H/m
$K = 22$ W/m·K	$\rho = 7200$ kg/m^3
$L = 3 \times 10^{-3}$ m	$\beta = 1 \times 10^{-4}$ K^{-1}
$T_\infty = 300$ K	$\gamma = 1.0$ N/m
$T_m = 1723$ K	$\partial\gamma/\partial T = -0.112 \times 10^{-3}$ N/mK
$\eta = 0.65$	

that the geometry of the weld pool can be sufficiently characterized using the parameters l, a, and b [14]. Also, the back-side bead width can be accurately calculated using l, a, and b [14]. Thus, these parameters are used to characterize the geometry of the weld pool.

4 Computational Results and Experimental Verifications

The governing equations with the boundary conditions are transformed into finite difference equations. In order to improve the accuracy of the calculation, $50 \times 50 \times 30$ unevenly spaced grids are used for the $50 \times 30 \times 3$ mm calculational domain. The minimum grid space was 0.4, 0.25, and 0.1 mm in the x-, y-, and z-directions, respectively. Fine spacing was used in the weld pool region because of the higher temperature gradient. The finest spacing was used for the thickness-direction in order to describe the deformed weld pool surface. The SIMPLER algorithm [24] is employed to calculate the temperature and fluid flow fields. Different welding parameters have been used in the calculation in order to analyze the effect of welding parameters on the geometry of weld pools. It is known that both σ_q and σ_q increase when the welding current or arc length is increased. In our calculation, σ_q and σ_q are determined for different welding current and arc length according to the experimental results [22]. Calculations are made for GTA weld pools on stainless steel (304) plates. The parameters used in the computation are shown in Table 1.

The calculated results of temperature distribution for partial penetration and full penetration are shown in Fig. 4 and Fig. 5, respectively. In Fig. 4(a), (b) and Fig. 5(a), (b), melting temperature is indicated using the dash-dot lines. The interval of temperature between the two adjacent lines is 250°K. The deformation of the top and bottom surfaces can be seen clearly. The top surface of the molten metal is concave in the plasma impacted region and is convex in the non-impacted region. The bottom surface of the molten pool is entirely concave downward. In Fig. 4(c), (d) and Fig. 5(c), (d), three-dimensional temperature distributions on the top and bottom surfaces for partial and full penetration are shown. On both the top and bottom surfaces, there are temperature peaks, and the temperature gradient ahead of the moving arc is larger than that behind the arc.

The calculated results of fluid flow in weld pools for partial and full penetration are shown in Figs. 6 and 7. It can be seen that in both partial and full penetration cases, there are similar patterns of fluid flow in weld pools, i.e., except for the pool edge, the molten metal on the surface flows radially outward and moves vertically upwards in the neighborhood of the arc axis. The maximum flow velocities are 0.62 m/s in Fig. 6, and 0.69 m/s in Fig. 7. It is known that buoyancy normally plays a less important role in determining the flow pattern than the temperature coefficients of the surface tension and electromagnetic force [25]. In our case, small currents, maximally 160 A, were used and the electromagnetic force is therefore relatively small. As a result, the pattern of convection in the weld pool is mainly determined by the temperature coefficient of the surface tension. That means that the geometrical appearance of the weld pool is also mainly determined by the temperature coefficient of the surface tension. For stainless steel, the temperature coefficient of the surface tension on the pool surface is usually negative. In this case, the highest surface tension is reached at the solid-liquid interface, while the surface tension of the weld pool at the arc center is the lowest. Consequently, the molten metal flows outward from the arc center. It can be seen that our results are consistent with the experimental observations of the

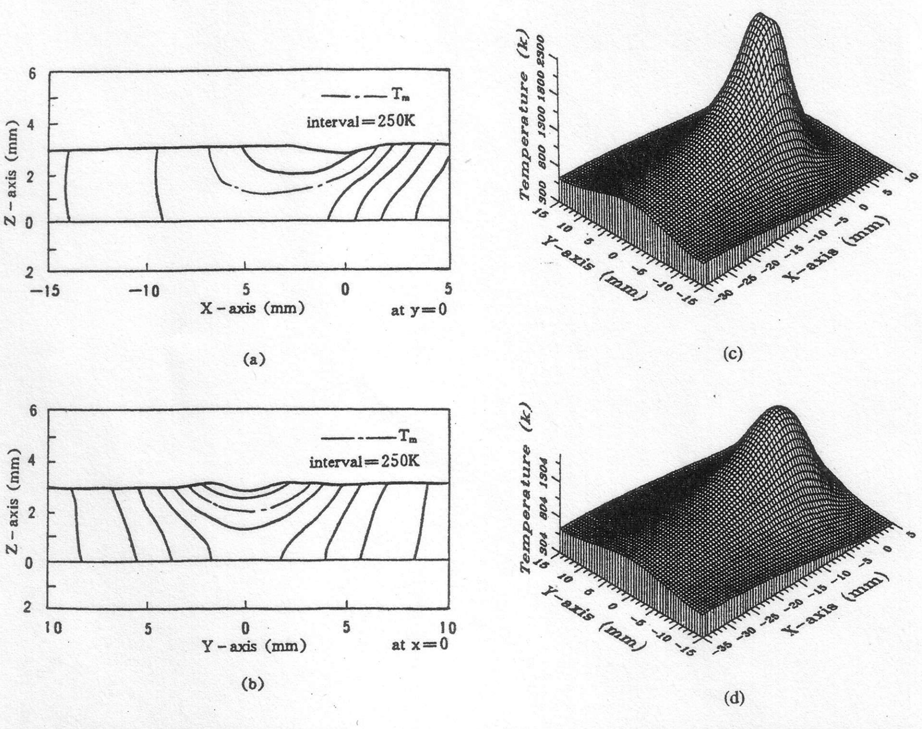

Fig. 4 Calculated temperature distribution with partial penetration. (a) Cross section; (b) longitudinal section; (c) top surface; (d) bottom surface (workpiece: stainless steel, welding parameters: 140A, 12V, 3.5 mm/s).

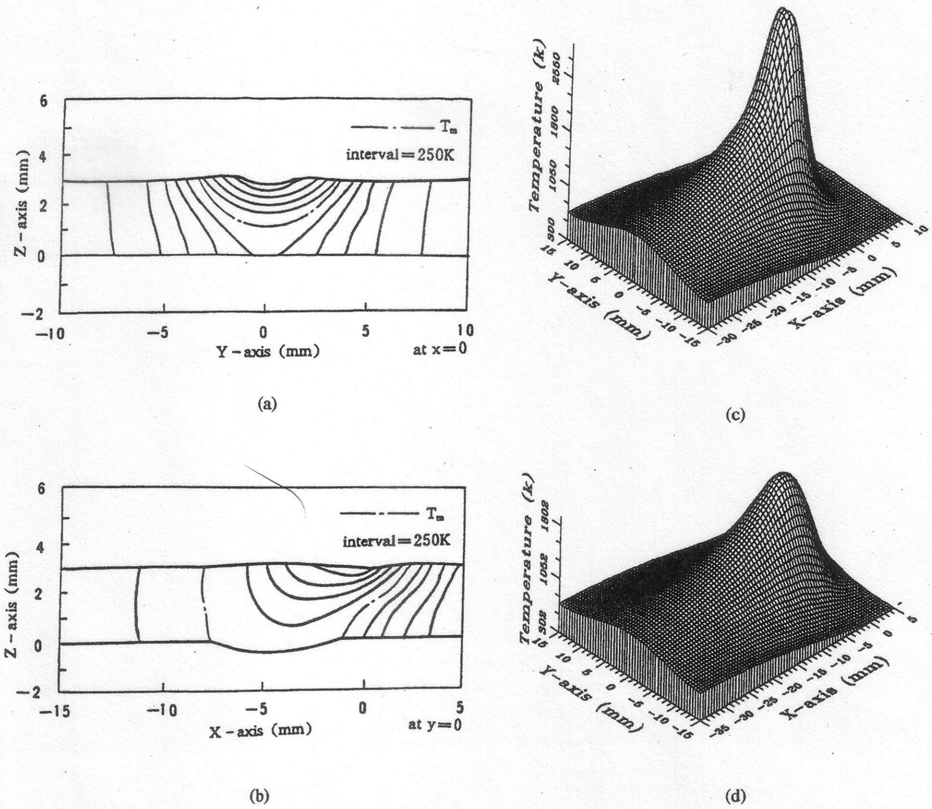

Fig. 5 Calculated temperature distribution with full penetration. (*a*) Cross section; (*b*) longitudinal section; (*c*) top surface; (*d*) bottom surface (workpiece: stainless steel, welding parameters: 160A, 12V, 3.5 mm/s).

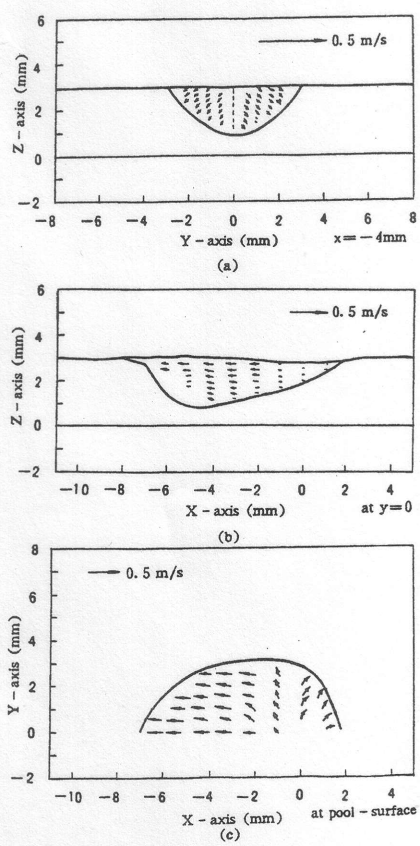

Fig. 6 Calculated fluid flow in weld pools with partial penetration. (*a*) Cross section; (*b*) longitudinal section; (*c*) top surface (workpiece: stainless steel, welding parameters: 140A, 12V, 3.5 mm/s).

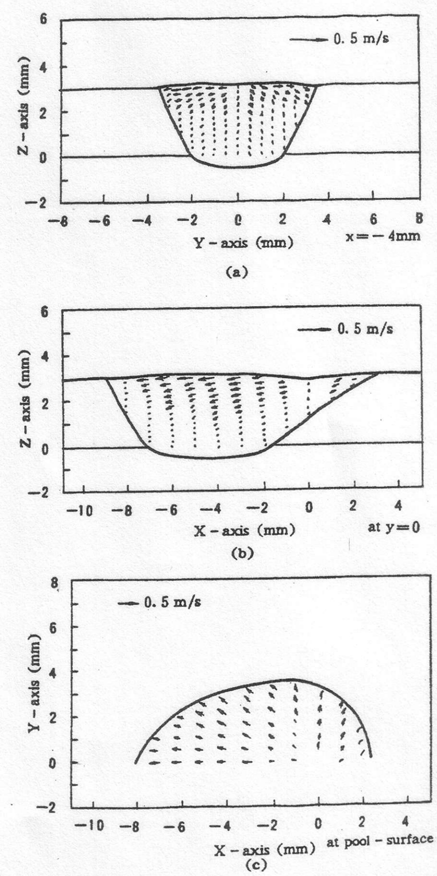

Fig. 7 Calculated fluid flow in weld pools with full penetration. (*a*) Cross section; (*b*) longitudinal section; (*c*) top surface (workpiece: stainless steel, welding parameters: 160A, 12V, 3.5 mm/s).

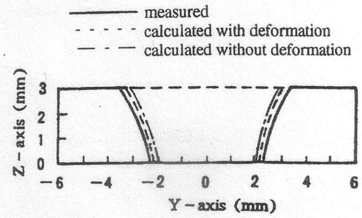

Fig. 8 Weld cross section comparison between calculation and experiment. (workpiece: stainless steel, welding parameters: 160A, 12V, 3.5 mm/s)

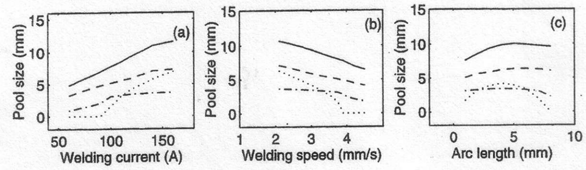

Fig. 10 Size of weld pools versus welding parameters (- length, -- width, .. back-side width, -. depth). (*a*) welding current (*b*) welding speed (*c*) welding arc length.

partially penetrated weld pools [26]. Hence, the small flow velocity on the bottom pool surface does not significantly affect the overall flow pattern in the weld pool.

GTA welding experiments are carried out for measuring the geometry of the weld pool and cross sectional shape of the weld in order to verify the validity of the numerical model. A comparison between calculated and experimentally obtained weld cross section is shown in Fig. 8. In Fig. 8, the solid line indicates the measured result, the dash-dot line represents the calculated result without consideration of pool surface deformation, and the dash line is the calculated one with consideration of pool surface deformation. The measured boundary was obtained from the macrograph of the weld cross section. It can be seen that predicted results with the consideration of pool surface deformation matches better with the experimentally observed ones.

A high-shutter speed camera assisted with pulsed laser illumination [11] is used to capture the clear image of the weld pool Fig. 9(*a*)–(*c*). The pool boundary is extracted by the developed real-time image processing algorithm [12]. Then the normalized models can be identified based on the extracted pool boundaries [14]. The comparisons between the calculated and measured weld pools are shown in the normalized coordinate system (Fig. 9(*d*)–(*f*)). It can be seen that the numerically calculated results are in good agreement with the measured ones.

5 Results and Discussion

The influence of welding parameters on width, length, and depth of the weld pool is shown in Fig. 10. The bead width, length, and depth (or the backside width) increase when increasing the current or decreasing the speed (Fig. 10(*a*), (*b*)). On the other hand, the effect of arc length on the bead width, length, and depth (or the backside width) is more complex (Fig. 10(*c*)). It seems that there is an optimal range of arc length for generating the maximum full penetration state (back-side bead width).

The effect of welding currents on geometrical appearance is shown in Fig. 11. The geometrical appearances of weld pools in the regular coordinate and the normalized coordinate systems are shown in Fig. 11(*a*) and (*b*), respectively. It is found that when increasing the welding current, the length of weld pool increases faster than the width. In order to analyze and compare the change in shape of weld pools (as shown in Fig. 11(*b*)), the weld pool lengths with different welding currents have been defined as the unit length (Its value equals 1). It is found that when increasing welding current, the trailing angle of the pool becomes smaller (sharper). In fact, when increasing welding current, the surface temperature over the whole weld pool area tends to increase quickly. However, due to the movement of the arc, the condition of heat transfer across the width of weld pools is better than the transfer condition along the length-direction. Therefore, the increase of heat energy from the increase in welding current will be consumed by increasing the length of weld pools more than by increasing the width of weld pools. This can also be seen in Fig. 10(*a*). Hence, by changing the welding current, it is possible to efficiently control the width to length ratio and the trailing angles of weld pools, which as noted in the introduction can significantly affect the grain structure. The above calculation results are currently being used to develop a control model.

The effect of welding current on the maximum width and arc center location is shown in Fig. 11(*c*). It can be seen that the change in distance between the pool rear (i.e. the point (0, 0) in Fig. 11(*b*)) and the arc center (described with the dash-dot line) has a complex trend as the current changes. When the current is low, the distance has a minimum value. After the weld pool is fully penetrated, the distance nearly remains constant. On the other hand, the distance between the pool rear and the location of maximum width (described with the solid line) always increases with the current. In addition, the trend of the change in distance between the arc center and the location of maximum width (described with dash line) is similar to that of the distance between the pool rear and the arc center.

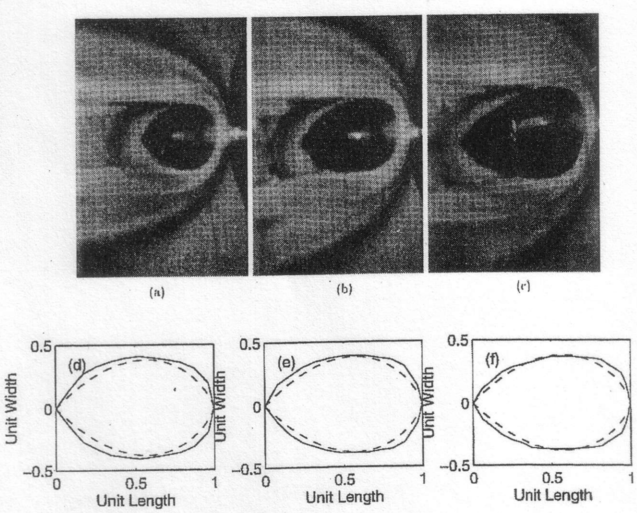

Fig. 9 Appearance geometry comparison of weld pools between calculation and measurement (- measurement, -- numerical calculation). (*a*)–(*c*) weld pool images (The images were acquired from the pool rear at 45 deg view angle [12].), (*d*)–(*f*) comparison between calculated and measured pool boundaries in the normalized coordinate. (*a*) and (*d*): 2.41 mm/s, (*b*) and (*e*): 1.95 mm/s, (*c*) and (*f*): 1.43 mm/s (workpiece: stainless steel, welding parameters: 100A, 12V, 3 mm arc length.)

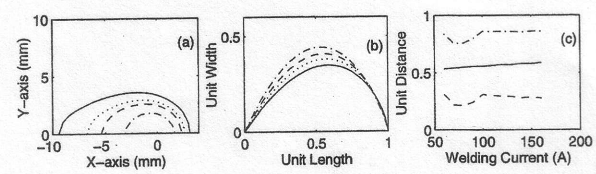

Fig. 11 Effect of welding currents on geometrical appearance of weld pools. (*a*) geometrical appearance of weld pools in regular coordinate (-. 60A, -- 100A, .. 120A, - 160A) (*b*) geometrical appearance of weld pools in normalized coordinate (-. 60A, -- 100A, .. 120A, - 160A) (*c*) locations of arc center and maximum width (-. arc center, - maximum width, -- distance between arc center and maximum width)

The effect of welding speeds on the geometry of weld pools is shown in Fig. 12. The geometrical appearances of weld pools in the regular coordinate and the normalized coordinate systems are shown in Fig. 12(*a*) and (*b*), respectively. The location of arc center and maximum width is shown in Fig. 12(*c*). It is found that when increasing the welding speed, the increases in the length of weld pool are almost the same as those in the width of weld pool. Similar results have also been acquired by experimentation (Fig. 9). This implies that the effect of welding speed on the shape is not significant. Thus, the welding speed can be adjusted to acquire the desired size of the weld pool. The control of the pool size and shape can be significantly simplified. On the other hand, it can be seen that the locations of the arc center and the maximum width in the normalized coordinate system remain nearly constant (Fig. 12(*c*)). This again shows that the influence of the welding speed on the shape of the weld pool is slight.

Effect of the arc length on the geometry of weld pool is shown in Fig. 13. The geometrical appearance of weld pool in the regular coordinate and the normalized coordinate systems are shown in Fig. 13(*a*) and (*b*). The locations of arc center and maximum width are shown in Fig. 13(*c*). It can be seen that the change in the pool size is significant when the arc length is less than 3 mm. However, when the arc length exceeds beyond 3 mm, the change in the pool size becomes slow. In addition to the size, the shape of the weld pool also changes with the arc length when the arc length is small. It can be seen in Fig. 13(*b*) that the weld pool becomes circular when the arc length decreases. Similarly, when the arc length further increases, its influence on the shape of the weld pool tends to be small (Fig. 13(*b*)). Compared with the current, the influence of the arc length on the shape is much smaller (Fig. 11(*b*) and Fig. 13). Also, the influence of the arc length on the size of the weld pool is much smaller than that of the welding speed. Thus, in the prospective control system of the weld pool geometry, the current and welding speed should be selected as the main control variables to adjust the size and shape of the weld pool. As the auxiliary variable, the arc length could be used to achieve a fine control system for the weld pool geometry. On the other hand, the locations of the arc center and maximum width change very slowly (Fig. 13(*c*)). In fact, when changing the arc length, the arc distributed region of heat, current, and pressure tends to change evenly. Therefore, the effect of arc length on geometrical appearance of weld pools is not significant.

6 Conclusion

A three-dimensional numerical model has been developed to describe the fluid flow and heat transfer in weld pools. Both the full penetration and the free surface deformation of weld pools on the top and bottom are considered. Temperature distribution and fluid flow field are obtained. GTA welding experiments are made to verify the validity of the numerical models. It is found that the calculated results have a good agreement with the experimental ones. In order to analyze the influence of welding parameters on the geometrical appearance of weld pools, a normalized model is developed to characterize the geometrical appearance of weld pools. Based on the numerical results, the following are found:

(1) The welding current can significantly affect the geometrical appearance. As the welding current increases, the curvature of the weld pool boundary at the trailing end increases.

(2) The effect of the welding speed on the geometrical appearance shape is slight. Whereas its influence on the pool size is great.

(3) In the interest range of arc length (from 1 mm to 4 mm), the arc length can affect both the size and the shape of the weld pool. However, compared with the welding current and speed, its influences are much weaker.

Thus, the welding current and speed could be selected as the main control variables for adjusting the geometrical appearance (size and shape) of the weld pool. The arc length could be used as an auxiliary control variable for a fine control of weld pool. Because of the weak influence of the welding speed on the weld pool shape, a decoupling control system could be easily developed to control the size and shape of the weld pool in order to achieve the desired weld grain structure.

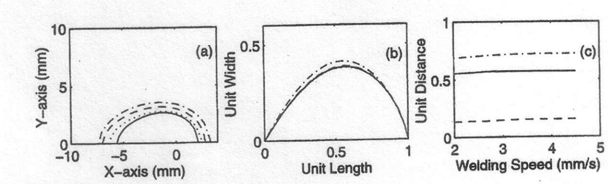

Fig. 12 Effect of welding speeds on geometrical appearance of weld pools. (*a*) Geometrical appearance of weld pools in the regular coordinate (-. 2.1 mm/s, -- 2.7 mm/s, .. 3.3 mm/s, - 3.9 mm/s) (*b*) geometrical appearance of weld pools in the normalized coordinate (-.2.1 mm/s, -- 2.7 mm/s, .. 3.3 mm/s, - 3.9 mm/s) (*c*) locations of arc center and maximum width (-. arc center, - maximum width, -- distance between arc center and maximum width)

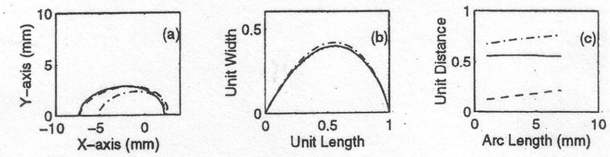

Fig. 13 Effect of welding arc lengths on geometrical appearance of weld pools. (*a*) Geometrical appearance of weld pools in the regular coordinate (-. 1 mm, - 3 mm, .. 5 mm, - 7 mm). (*b*) geometrical appearance of weld pools in the normalized coordinate (-. 1 mm, - 3 mm, .. 5 mm, - 7 mm). (*c*) locations of arc center and maximum width (-. arc center, - maximum width, — distance between arc center and maximum width)

Acknowledgment

This work is supported by the National Science Foundation (DMI-9412637 and DMI-9414530) and Allison Engine Company, Indianapolis, IN.

References

1 Kou, S., and Le, Y., 1985, "Grain Structure and Solidification Cracking in Oscillated Arc Welds of 5052 Aluminum Alloy," *Metall. Trans.*, Vol. 16A, p. 1345.

2 Kou, S., and Le, Y., 1985, "Alternating Grain Orientation and Weld Solidification Cracking," *Metall. Trans.*, Vol. 16A, p. 1887.

3 Kou, S., and Le, Y., 1985, "Improving Weld Quality by Low Frequency Arc Oscillation," *Weld. J.*, Vol. 64, p. 51.

4 Kou, S., and Le, Y., 1988, "Welding Parameters and the Grain Structure of Weld Metal—A Thermaldynamic Consideration," *Metall. Trans.*, Vol. 19A, p. 1075.

5 Savage, W. F., Lundin, C. D., and Aronson, A. H., 1965, "Weld Metal Solidification Mechanics," *Weld. J.*, Vol. 44, pp. 175s.

6 Savage, W. F., and Aronson, A. H., 1966, "Preferred Orientation in the Weld Fusion Zone," *Weld. J.*, Vol. 45, p. 85s.

7 Savage, W. F., Lundin, C. D., and Chase, T. F., 1968, "Solidification of Fusion Weld in Face-Centered Cubic Metals," *Weld. J.*, Vol. 47, p. 522s.

8 Savage, and Hrubec, R. J., 1972, "Synthesis of Weld Solidification Using Crystalline Organic Materials," *Weld. J.*, Vol. 51, p. 260s.

9 Zhang, Y. M., et al., 1993, "Determining Joint Penetration in GTAW with Vision Sensing of Weld-Face Geometry," *Weld. J.*, Vol. 72, p. 463s.

10 Zhang, Y. M., Kovacevic, R., and Wu, L., 1996, "Dynamic Analysis and Identification of Gas Tungsten Arc Welding Process for Full Penetration Control," ASME *Journal of Engineering for Industry*, Vol. 118(1), p. 123–136.

11 Hoffman, T., 1991, "Real-Time Imaging for Process Control," *Advanced Material and Process*, Vol. 140, p. 37.

12 Kovacivic, R., Zhang, Y. M., and Ruan, S., 1995, "Sensing and Control of Weld Pool Geometry for Automated GTA Welding," ASME *Journal of Engineering for Industry*, Vol. 117, p. 210–222.

13 Kovacevic, R., Zhang, Y. M., and Li, L., 1996, ''Monitoring of Weld Penetration Based on Weld Pool Geometrical Appearance,'' to appear in Research Supplement, *Weld. J.*

14 Zhang, Y. M., Li, L., and Kovacevic, R., 1995, ''Dynamic Estimation of Full Penetration Using Geometry of Adjacent Weld Pools,'' ASME *Journal of Engineering for Industry,* Submission.

15 Zacharia, T. et al. ''Three-Dimensional Transient Model for Arc Welding Process,'' *Metall. Trans.,* Vol. 20B, p. 645.

16 Thompson, M. E., and Szekely, J., 1989, ''The Transient Behavior of Weld Pools with a Deformed Free Surface,'' *Inter. J. of Heat and Mass Transfer,* Vol. 32, p. 1007.

17 Choo, R. T. C., and Szekely, J., 1990, ''Modeling of High-Current Arc With Emphases on Free Surface Phenomena in the Weld Pool,'' *Weld. J.,* Vol. 69, p. 223s.

18 Tsai, M. C., and Kou, S., 1989, ''Marangoni Convection in Weld Pools With a Free Surface,'' *Inter. J. of Numerical Methods in Fluid,* Vol. 9, p. 1503.

19 Kim, J. W., and Na, S. J., 1994, ''A Study on the Three-Dimensional Analysis of Heat and Fluid Flow in Gas Metal Arc Welding Using Boundary-Fitted Coordinates,'' ASME *Journal of Engineering for Industry,* Vol. 116, p. 78.

20 Kim, S. D., and Na, S. J., 1992, ''Effect of Weld Pool Deformation on Weld Penetration in Stationary Gas Tungsten Arc Welding,'' *Weld. J.,* Vol. 71, p. 179s.

21 Ohji, T., and Nishiguchi, K., 1983, ''Mathematical Modelling of Molten Pool in Arc Welding of Thin Plate,'' IIW DOC.211-555-83.

22 Tsai, N. S., and Eagar, T. W., 1985, ''Distribution of the Heat and Current Flues in Gas Tungsten Arcs,'' *Metall. Trans.,* Vol. 16B, p. 841.

23 Choi, M., and Greif, R., 1987, ''A Study of the Heat Transfer During Arc Welding With Applications to Pure Metals Temperature Materials,'' *Numerical Heat Transfer,* Vol. 11, p. 477.

24 Patankar, S. V., 1980, *Numerical Heat Transfer and Fluid Flow,* McGraw-Hill, NY.

25 Woods, R. A., and Milner, D. R., 1971, ''Motion in the Weld Pool in Arc Welding,'' *Weld. J.,* Vol. 50, p. 163s.

26 Heiple, C. R., and Roper, J. R., 1982, ''Mechanism for Minor Element Effects on GTA Fusion Zone Geometry,'' *Weld. J.,* Vol. 61, p. 97s.